Geometry Induced Bias in the Remote Near-IR Identification of Phyllosilicates on Space Weathered Bodies

Stefano Rubino, Sandra Potin, Cateline Lantz, Donia Baklouti, Pierre Beck, Olivier Brissaud, Hugues Leroux, Eric Quirico, Bernard Schmitt, Ferenc Borondics, et al.

To cite this version:

Stefano Rubino, Sandra Potin, Cateline Lantz, Donia Baklouti, Pierre Beck, et al.. Geometry Induced Bias in the Remote Near-IR Identification of Phyllosilicates on Space Weathered Bodies. Icarus, 2022, Icarus, 376, pp.114887. 10.1016/j.icarus.2022.114887 . hal-03696309

HAL Id: hal-03696309
https://hal.univ-lille.fr/hal-03696309v1

Submitted on 22 Jul 2024

Version of Record: https://www.sciencedirect.com/science/article/pii/S0019103522000094
Manuscript_703c10ddcd0c2611f63683d9c0c3bb93

Geometry Induced Bias in the Remote Near-IR Identification of Phyllosilicates on Space Weathered Bodies

Stefano Rubino[1], Sandra Potin[2], Cateline Lantz[1], Donia Baklouti[1], Pierre Beck[3], Olivier Brissaud[3], Hugues Leroux[4], Eric Quirico[3], Bernard Schmitt[3], Ferenc Borondics[5] and Rosario Brunetto[1]

[1] Institut d'Astrophysique Spatiale, Université Paris-Saclay, CNRS, F-91405, Orsay, France; stefano.rubino@ias.u-psud.fr
[2] Laboratoire d'Etudes Spatiales et d'Instrumentation en Astrophysique (LESIA), Observatoire de Paris, Université PSL, CNRS, Sorbonne Université, Université de Paris, 5 place Jules Janssen, 92195 Meudon, France
[3] Université Grenoble Alpes, CNRS, IPAG, 414 rue de la Piscine, 38400 Saint-Martin d'Hères, France
[4] Univ. Lille, CNRS, INRAE, Centrale Lille, UMR 8207—Unité Matériaux et Transformations, F-59000 Lille, France
[5] SMIS Beamline, SOLEIL Synchrotron, Gif sur Yvette Cedex, France

Abstract

Sample return missions Hayabusa2 (JAXA) and OSIRIS-REx (NASA) found evidence of hydrated silicates on the surface of C and B-type asteroids Ryugu and Bennu. This detection relied on the study of the 2.7 µm OH-stretching spectral feature revealed from remote sensing observations of the asteroids' surfaces. Laboratory studies simulating the effects of space weathering (SpWe) on primitive bodies have shown that the feature's position, considered as the wavelength of the band minimum, can vary under ion implantation, shifting towards longer wavelengths for implanted surfaces. Since SpWe is a surface process, we investigated how the geometry of observation can affect the hydration feature on space weathered surfaces. Here, we report new laboratory Reflectance Factors (REFF) measurements on pristine and ion-bombarded phyllosilicate pellets, to monitor the evolution of the 2.7 µm feature with varying observation geometry. We found that, as we approach specular reflection, the feature's position for He+ bombarded surfaces shifts towards longer wavelengths. We interpret that the spectral shift is due to chemical and physical changes induced by ion implantation in the first hundreds of nanometers of our phyllosilicate pellets. The diversity in the observed amplitude of the shift means that different competing effects are dominating at different optical configurations, mainly volume and surface scattering. The effects of the ion-implanted matter are especially visible when measuring in near-specular conditions, where the specular component (more sensible to the very top surface (implanted layer) of the sample)dominates - hence the larger shift measured. Our results indicate that the geometry of observation can induce a certain bias in the interpretation of remote sensing data from space-weathered bodies.

---

[1] Corresponding author stefano.rubino@ias.u-psud.fr

1. INTRODUCTION

A correct interpretation of the hydration features on small bodies is paramount in understanding the evolution of primitive materials in the early Solar System. It is particularly relevant in the context of the two sample-return missions Hayabusa2 (JAXA) and OSIRIS-REx (NASA), targeting the C-type asteroid (162173) Ryugu (Watanabe et al. 2017) and the B-type asteroid (101955) Bennu (Lauretta et al. 2017), respectively. Hayabusa2 successfully collected material from the surface of its target first in February 2019, then in July 2019, and brought back several grams of Ryugu grains to the Earth, on Dec. 6 2020. OSIRIS-REx has also performed sample collection from its target's surface in October 2020, and the spacecraft is now in the next phase of the mission, Earth Return Cruise, starting in March 2021. Besides sample collection, both missions performed extensive spectroscopic surveys in both the visible and the near-IR of their target's surfaces, using the NIRS3 (Near Infrared Spectrometer, (Iwata et al. 2017) and OVIRS (OSIRIS-REx Visible and InfraRed Spectrometer, (Christensen et al. 2018) instruments, respectively. They detected a band at $2.72\ \mu m$ on Ryugu (Kitazato et al. 2019) and at $2.74\ \mu m$ on Bennu (Hamilton et al. 2019), associated with the stretching vibration of hydroxyl groups (-OH) covalently bonded to metallic atoms (M) in phyllosilicates. The position and the shape of this hydration feature can vary with mineral composition and structure (Madejová, Gates, and Petit 2017). The $2.7\ \mu m$ feature has been studied in carbonaceous chondrites (Takir et al. 2013), but it has also been detected on outer space bodies, such as the dwarf planet Ceres (De Sanctis et al. 2015) and some other low-albedo objects (such as C-class and related asteroids - (Jones et al. 1990; Usui et al. 2018; Rivkin et al. 2002). On Bennu, the feature appears to be deep and broad, similar in shape to laboratory spectra of some carbonaceous chondrites. However, Ryugu's feature is significantly weaker and narrower, indicating a different degree of surface hydration and/or a different thermal history (Kitazato et al. 2021). Hayabusa2 also conducted an impact experiment using the Small Carry-on Impactor (SCI). Results are described by (Arakawa et al. 2020) and the subsurface material NIRS3 observations are presented by (Kitazato et al. 2021). The excavated material exhibits a $2.7\ \mu m$ feature that appears stronger and slightly blueshifted in comparison to the one observed for the surface. Space weathering (SpWe) could explain these observations: SpWe affects atmosphere-less bodies in our solar system by multiple processes, such as micrometeorite bombardment, high-energy cosmic irradiation and solar wind bombardment, with both high and low energy ions (Beth Ellen Clark et al. 2002; Brunetto et al. 2015). SpWe can alter the physical and chemical structure of surface materials on asteroidal bodies, inducing variations of their spectral properties (B. E. Clark et al. 2001; Ishiguro et al. 2007). Recent attempts to reproduce solar wind SpWe in the laboratory, both on carbonaceous chondrites (CCs) (Lantz et al. 2015, 2017; Brunetto et al. 2020) and on hydrated terrestrial silicates (Rubino et al. 2020), have shown that the $2.7\ \mu m$ feature in native hydrated silicates appears at shorter wavelengths than in ion-bombarded samples, similarly to the observation by NIRS3 on the SCI crater on Ryugu. However, recent studies have shown that the geometrical configuration of an observation can affect the shape of the hydration feature in carbonaceous chondrites (S. Potin et al. 2019). Remote sensing instruments onboard space missions often observe objects at different times and angles, in a way that the same area is measured at various geometries. Thus, it is important to investigate and understand how the geometry of the observation can affect the hydration feature on space weathered surfaces. To address this question, we report new experimental Reflectance Factor (REFF) measurements on pristine and ion-bombarded phyllosilicate pellets, aimed at monitoring the evolution of the $2.7\ \mu m$ feature with varying observation geometry.

2. SAMPLES AND METHODS

2.1 Samples description and preparation

The new REFF measurements were done on the phyllosilicate pellets used by Rubino et al. (2020), which underwent He^+ and Ar^+ ion bombardment at $40\ keV$, at room temperature and $P \sim 10^{-7}$mBar, with an ion fluence of $6 \cdot 10^{16}$ ions/cm^2 for He^+ and $2 \cdot 10^{16}$ ions/cm^2 for Ar^+. The relevance and the limitations of He^+ and Ar^+ ion-bombardment at $40\ keV$ as a simulation of solar wind irradiation are presented in the paper preceding this work, Rubino et al. (2020), and further discussed by Brunetto et al. (2014) and Lantz et al. (2017).

The measurements presented in this work were performed on a serpentine sample. Serpentines are among the major hydrated silicates phases found in CI- and CM-type chondrites (King et al. 2015) and can be used as analogs for the surface of primitive hydrated bodies such as Ryugu and Bennu (Kitazato et al. 2019; Hamilton et al. 2019). Our serpentine was extracted from the Rawhide mines, in California. It will thus be referred to as Serpentine Rawhide. This sample is mostly antigorite with chrysotile veins, with a $Fe/(Fe+Mg)$ ratio equal to 0.07.

The sample was crushed using an agate mortar. The grain size of the resulting powder was estimated by scanning electron microscopy (SEM), and was found in the range $1\text{-}100\ \mu m$. Three pellets were made by pressing $\sim 240\ mg$ of powdered sample onto a PEG substrate (powdered polyethylene glycol with an average molecular mass of *8000 g/mol*, from Fisher Scientific), for a duration of *5* minutes, using a *7*-tons press. We made three pellets, two of them underwent ion-bombardment, while the third/last pellet was preserved as a control sample. The pellets have a somewhat flat surface, which is expected to produce strong specular effects. Additional details about the samples and sample preparation can be found in Rubino et al. 2020.

It is relevant to note that meteorites are generally used as analogue materials for asteroidal surfaces. And in fact, ion-implantation experiments have already been conducted on meteorites (see Brunetto et al. 2014, Lantz et al. 2015-2017). However, meteorites can also be very heterogeneous materials, especially at the scale we are working here (mm to fractions of microns). This heterogeneity may introduce other effects in our measurements, which may not be well constrained. This may hinder the efforts in deriving a sort of “general behavior" of hydrated silicates under ion-bombardment, hence the choice in this work of focusing on pure (or almost pure) phyllosilicate phases.

2.2 Experimental setup

2.2.A Reflectance Factor (REFF)

We performed the REFF measurements with the SHADOWS (Spectrophotometer with cHanging Angles for the Detection Of Weak Signals) spectro-gonio radiometer at the Université of Grenoble Alpes (Sandra Potin et al. 2018). This instrument allows acquiring spectra in the visible and near infrared range (*350-5000 nm*) at different observation geometries. A monochromatic beam is focused on the sample’s surface, with beam-size of approximately *5.2 mm* in diameter for a nadir illumination (normal to the surface). The reflected light is measured by two detectors, covering the visible and near-infrared ranges, mounted on a rotating arm. The illumination and the observation angles are defined with respect to the normal to the surface and can be changed, which allows us to automatically acquire spectra for different observation geometries. For our measurements, we set four illumination angles : *0*°, *20*°, *40*° and *60*°, with an angular resolution of ±*2.9*°. For each illumination angle, we acquired a series of spectra by varying the observation angle, from *-70*° to *70*°, with a *10*° step and an angular resolution of ±*2.05*°, exploring all geometrical configurations except opposition geometry. For each sample, using these parameters, a total of 56 geometrical configurations were explored. The spectral sampling and the evolution of the spectral resolution in our spectra are shown in appendix A. This parameter set configuration resulted in approximately 13h of acquisition per sample. The reflectance factor is calculated during the measurement by comparison with a Spectralon (99% reflectance, Labsphere) and Infragold (Labsphere) reflectance targets, taking into account the Reflectance Factors (REFF) of the references, meaning that the reference is measured at the same observation geometry of the sample. The reflectance of the samples is thus compared to a lambertian surface, by dividing the measured spectra with the reference spectra. In this configuration, reflectance values above 1 for specular configuration on very flat surfaces are to be expected.

2.2.B Scanning Electron Microscopy imaging

After spectroscopic measurements, Scanning Electron Microscopy SEM studies were conducted at the University of Lille, France. A thin coating of carbon was deposited over the pellet surface to perform high resolution secondary electron imaging at 3 keV, using a JEOL JSM-7800F at a working distance of *10 mm*. High magnification images of the pellets' surfaces were acquired to visualize changes in the surface topography due to ion implantation.

3. RESULTS

3.1 Main spectral features

Almost all the acquired spectra show the same absorption bands (shown in Figure 1):

- a deep 2.7 µm band associated as with the (M)-OH stretching vibration ;
- a broad 3 µm shoulder, which can be a combination of structural and adsorbed water bands (in this sample, minor amounts of structural water are expected, so this contribution is probably dominated by the contribution of adsorbed water) , as well as CH stretching bands around 3.4 µm ;
- overtones and combination mode peaks of water molecules at 1.4 and 1.9 µm (Ryskin 1974; Ockman 1958) ;
- two additional bands at 2.3 and 2.5 µm, originated from the stretching vibrations of Mg-OH and/or Fe-OH (Clark et al. 1990).

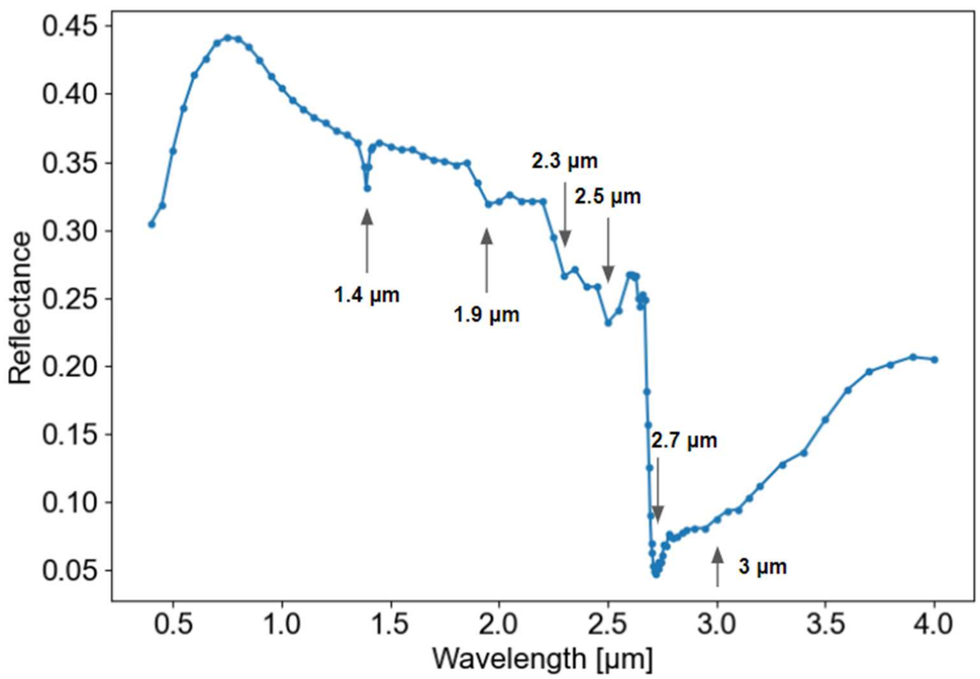

Figure 1. Example of acquired spectra – He^+ implanted pellet at $(i, e) = 20°, 40°$)

Generally speaking, the first effect we notice is a change in the shape of the hydration band at $2.7\mu m$, which gets sharper as we approach the specular reflection geometry (see Figure 2). For some configurations, when looking at the whole dataset (see Appendix B, figure B1), approaching specular geometry, strong features seem to sharpen while less intense ones seem to shrink.

We also note that due to a possible increase of the contribution from specular reflection, spectra from these configurations also could exhibit the spectral signature of the real refractive index from the top layer. This can happen because the real part of the refractive index n always oscillates like a derivative around a band (see Kramers-Kronig relations -) and is always lower before the band peak and higher after: thus the specular contribution is lower and then higher. This induces a negative (or blue) shift of the 'apparent absorption' peak position when added with the multiple scattering contribution. This signature would corresponds to the slight bump after the 2.7 µm feature (at approximately 2.715 µm) , and the tiny blue-shift of the 2.7 µm band, visible in the non-bombarded sample (the position of the feature shifts from 2.705 µm for [$i = 60°$, $e = 0°$] to 2.700 for [$i = 60°$, $e = 60°$] - note that the spectral sampling here corresponds to $5\ mm$). For reference, the complex refractive index spectrum in serpentines to illustrate the optical constant's behavior can be found in Mooney and Knacke (1985).

Delving a bit deeper, while focusing on the hydration band, different behavior can be seen for the different cases :

- For the non-bombarded sample, the most prominent effect is the change in the shape of the hydration band. Approaching near-specular configuration, the feature gets sharper. Moreover, as the incidence angle *i* grows, for large phase angles, the apparent blue-shift due to the influence of the optical constants described above get more notable ;
- For the Ar^+ bombarded sample, the sharpening effect described above can also be seen in near-specular configurations. The slight shape change effect due to the influence of the optical constants is also noticeable for the $i = 60°$ case, although less intense ; there also seems to be a slight band position variability of the hydration feature (see section 3.2 for a detailed explanation);
- For the He^+ bombarded sample, the shape of the hydration band isn't affected by observation geometry as strongly as in the cases described above (or even at all) ; however, we can see a clear global band red-shift in the position of this band with respect to the other samples. The extent and evolution of this shift is further discussed in section 3.2.

These effects are better seen in the complete dataset, shown in Appendix B. We note that for all observations of the ion implanted samples in particular geometric configurations, the shape and position of the hydration feature can be considerably altered (Figure 2, panel c) with respect to the non-implanted pellet (Figure 2, panel a).

Finally, we note that the curves in panel (a) of Figure 2 are fairly asymmetric with respect to the emergence angle. This may be due to slight uncertainty in the position of the detector and slight differences on the observation spot position for symmetric emergence angles, possibly coupled to some lateral heterogeneity of the sample.

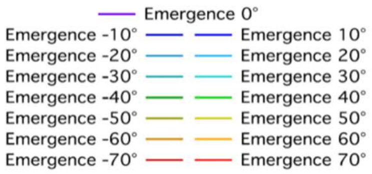

(a) Spectra from the **non-bombarded pellet** at different observation geometries

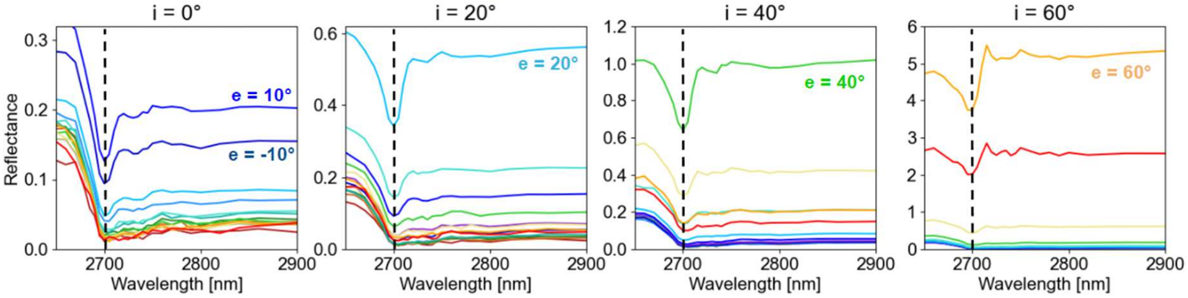

(b) Spectra from the **Ar+ implanted pellet** at different observation geometries

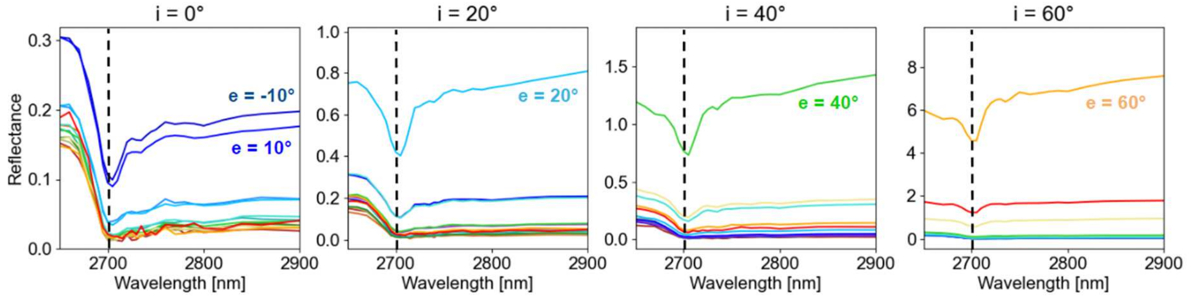

(c) Spectra from the **He+ implanted pellet** at different observation geometries

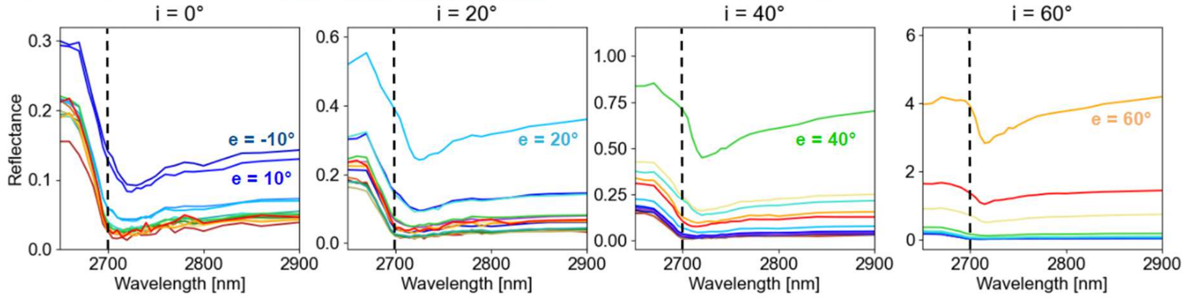

Figure 2. Detail of the REFF measurements centered around the hydration band (complete dataset but restricted to *2.65-2.9 μm*). The dashed line is precisely at 2.7 μm, and is used to gauge the evolution of the 2.7 μm feature's position.

3.2 REFF dataset results

We quantified the changes of the hydration feature at *2.7 μm* with varying optical geometries. To determine the two spectral parameters of interest, the peak position and the band depth, we applied the same method as in our previous work (Rubino et al. 2020). We first removed a linear continuum from *2.6* to *4 μm*. The continuum-removed spectra, centered on the hydration feature, are shown in the Appendix B, Figure B2. We then applied different instances of a Savitzky-Golay filter, using different windows-size values, to slightly smooth our data while taking in account different band shapes and degrees of noise correction. For each smoothed spectrum, we defined a region of interest (ROI) centered on the band and computed the barycenter associated to this spectral ROI to account for the asymmetry of the spectral feature. Finally, we averaged the wavelength obtained on each Savitzky-Golay instance and associated this value with the band position. Since the Savitzky-Golay filter acts as a sort of data interpolation process, by taking in consideration multiple instances of it, the computed positional value is very precise, with an improved accuracy with respect to spectral sampling and resolution (which still need to be taken in account when discussing the overall accuracy of the measurement). This method allowed us to extract the band position for all observation geometries. The band depth is calculated as $1 - R_{\mathrm{Band}}/R_{\mathrm{Continuum}}$, at the wavelength corresponding to the center of the band, and considering a linear continuum between the two inflection points of the band. The position values are shown in the polar plots of Figure 3.

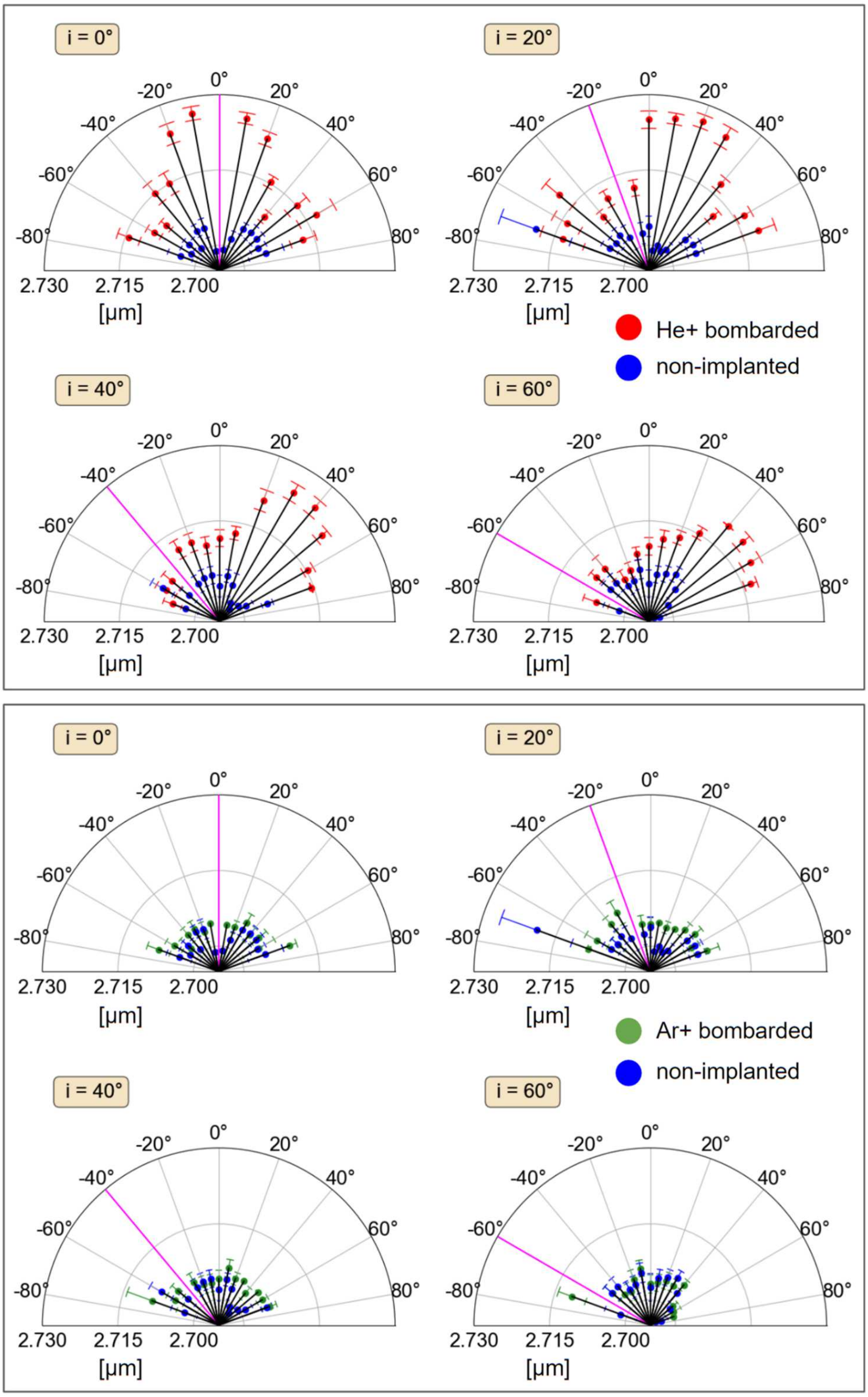

Figure 3. Evolution of the *2.7* μm hydration feature position under different optical geometries for He^+ and Ar^+ implanted pellets, with respect to the non-implanted pellet. The magenta line represents the direction of the illumination angle *i*. The plot shows the evolution of the *2.7* μm peak position as a function of the observation angle *e*, for fixed illumination angles *i*. In the polar plots, the observation angle *e* increases clockwise, while the illumination angle *i* increases counter-clockwise (scale not reported). The data from the ion implanted pellets (red for He^+ and green for Ar^+) are compared with data from the pristine pellets (in blue).

For the He^+ implanted pellets, the irradiation-induced spectral shift at longer wavelengths can be seen in all optical configurations. The amplitude of this shift can vary from a few nanometers to a maximum of *28 ± 2 nm.* The maximum is reached when observing in a specular configuration, with an angular width of about +/-20° (i.e., $e \sim i \pm 20°$). It is interesting to observe that for the large illumination angles, $i \sim 40°$ and $60°$, the spectral shifts increase also when $i \sim -e$: this might possibly be suggestive of backscattering effects. For the Ar^+-implanted pellets, the spectral shift at longer wavelengths with respect to the non-bombarded sample is less pronounced and can only be observed in specular configurations, where its amplitude is close to *6 nm*. Overall, the spectral resolution of our dataset does not allow us to efficiently distinguish between an Ar+ implanted pellet and a pristine one in most non-specular optical configurations. Looking at the positional data from the non-bombarded pellet, we can also spot the effect described in 3.1, where for specular geometries the specular component start to dominate the spectra, and the spectral signature from the real refractive index can be seen affecting the peak position, slightly blue-shifting it in these configurations. The evolution of the $2.7\,\mu m$ band depth (Figure 4) was also measured in a similar manner to the band position. It is relevant to note that commenting band-depth value in reflectance spectra on particularly bright surfaces can be quite delicate. As discussed by Milliken et al. (2007), band depth and apparent absorbance values can be correlated to albedo when derived from reflectance spectra. In the case of our study, the direct measure of band depth can be biased, especially approaching specular configurations, due to the measured albedo. This complicates the interpretation of this spectral parameter. However, this study highly focuses on the position of the hydration feature and its evolution upon ion-implantation. Results on band-depth are still reported here.

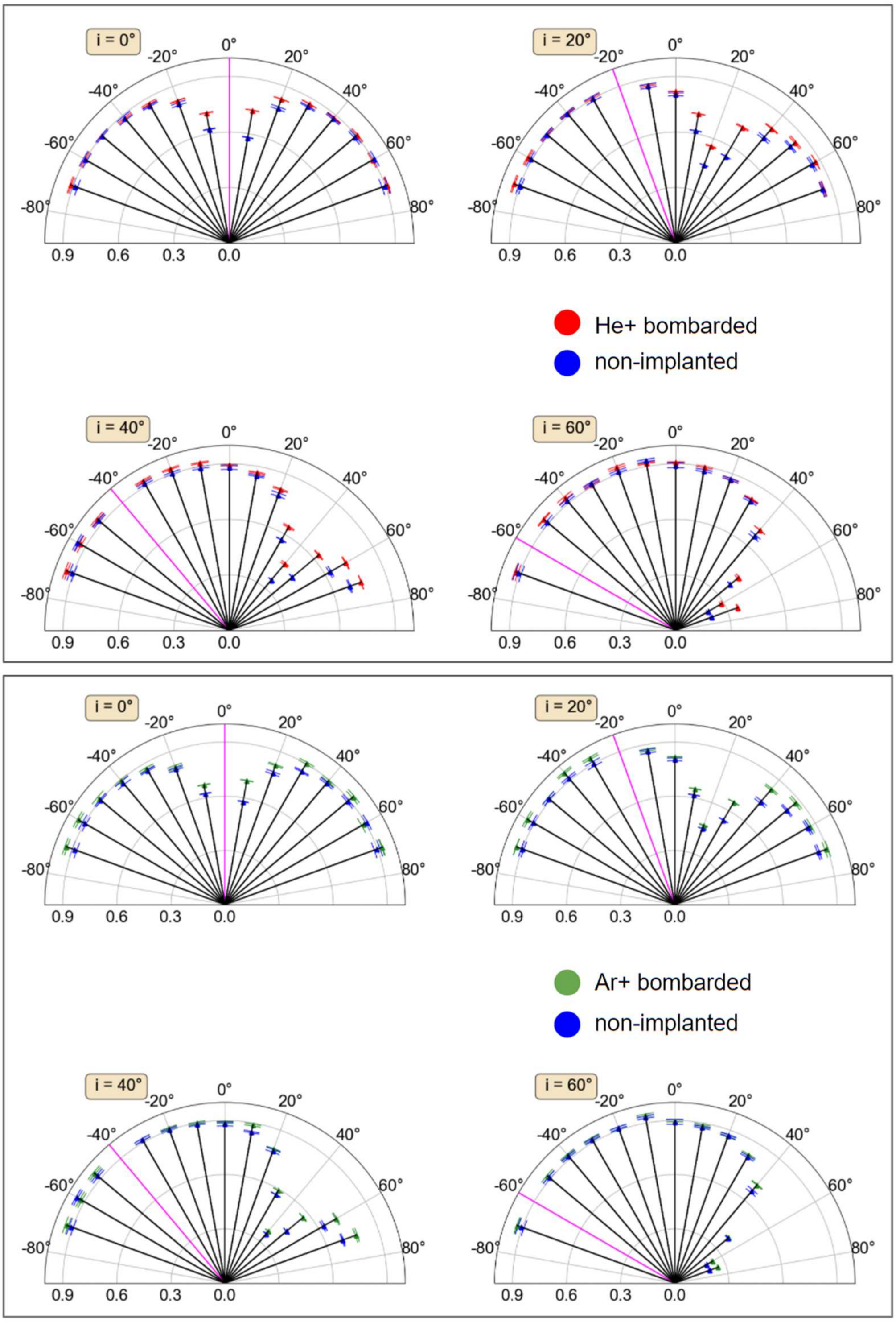

Figure 4. Evolution of the 2.7 μm hydration feature depth under different optical geometries for He^+ and Ar^+ implanted pellets, with respect to the non-implanted pellet.The magenta line represents the direction of illumination which corresponds to the incidence angle.

For all pellets, the $2.7\ \mu m$ band depth decreases in amplitude when approaching the specular configuration. For a fixed geometrical configuration, the hydration feature measured on both the implanted pellets is deeper than for the pristine pellet. In specular configurations (or approaching specular-like, for $i = 0$), the $2.7\ \mu m$ band depth in the He^{+} implanted pellets is ~30% deeper than in the pristine pellet. In the Ar^{+} implanted pellets, the band intensity is only ~15% deeper than in the pristine pellet.

3.3 EMG modeling findings

It is important to address that the hydration feature in phyllosilicates can incorporate multiple contributions depending on the complexity of the phyllosilicate sample. Structural and adsorbed water can also have a spectral signature near $3\ \mu m$, which can contribute to the broad spectral band at $3\ \mu m$. The quantification of these contributions and their evolution can be accessed by Exponentially Modified Gaussian (EMG) modeling (Grushka 1972; S. Potin et al. 2020). In Figure 5, we show the modeling of the various components of the broad spectral feature at $3\ \mu m$, before and after bombardment by He^{+}. This EMG modeling is first applied to spectra from Rubino et al. (2020), that we acquired with an Agilent Cary 670/620 micro-spectrometer installed at the SMIS beamline of the SOLEIL synchrotron (France), using a Schwarzschild objective with a numerical aperture of 0.81. We measured IR spectra using the internal Globar source, with respect to gold references, following the same procedure described by (Brunetto et al. 2018). Spectra were baseline-corrected and normalized using a linear continuum between 2.6 and $4\ \mu m$.

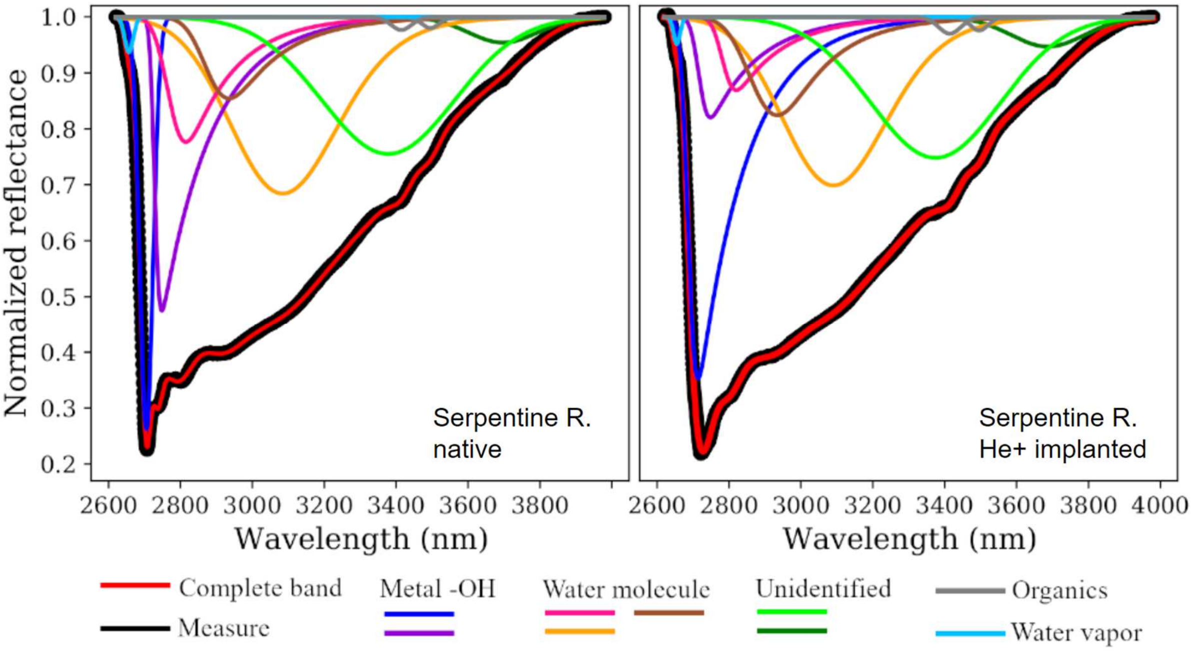

Figure 5. Comparison of the components forming the band at 3 µm before and after ion implantation on a pellet of Serpentine Rawhide, measured on an IR micro-spectrometer using Schwarzschild objective with a numerical

aperture of 0.81. The values are normalized considering a linear continuum around the absorption band. Fitting values from EMG modeling and their associated errors are shown in table C1 in Appendix C.

The high spectral resolution (4 cm^{-1}) and dense spectral sampling of these measurements allow the precise detection of various components in the band. The large absorption band at $3\ \mu m$ is a combination of several features, each tracing the presence of a -OH group bearer, plus the nearby features around $3.4\ \mu m$ due to $-CH_2$ and $-CH_3$ aliphatic groups. The various detected components could be due to a metal-OH group in a hydrated mineral, or water molecules. Variations in band depth, position of the minimum and FWHM are the results of modifications in the number of hydroxyl groups, as well as in the crystal structure of the minerals, as shown by previous investigations (Bishop et al. 1994, Frost et al. 2000, Kuligliewicz et al. 2015, Potin et al. 2020b). A shift upon ion-bombardment in the position of the minimum and/or broadening of the band with respect to the non-bombarded sample may indicate a distortion of the crystal lattice, bringing the -OH groups closer or further, so modifying their oscillation frequency. Band depth, position of reflectance minimum, and Full-Width at Half Maximum (FWHM), for the complete band and each component before and after bombardment, can be found in Appendix C.

It is important to note that the profile of the global band observed on both measurements is still recognizable between the two measurements, with the band depth only augmented by 0.8%, a band position shift of 20 nm toward the longer wavelengths and a decrease of the FWHM of 8 nm upon ion-bombardment. However, the various components of the spectral feature can be highly altered, such as the metal-OH component at 2.715 μm, losing 9% of depth, shifting of 105 nm toward the longer wavelengths and thinning of 17 nm. It is relevant to keep in mind that the components identification in the case of the ion-bombarded sample can be complicated by the disordering induced by the ion-implantation and the fact that the spectra associated to the bombarded sample is probably a mix of both bombarded and non-bombarded sample.

Based on the results of the EMG algorithm on the microspectrometer data, we applied EMG modeling to the REFF measurements. However, since REFF measurements have a lower spectral sampling and resolution than the spectra acquired with the microspectrometer, the algorithm is able to separate and quantify only four components, some being the combination of the previous detected components too close to each other to be accurately separated with this spectral resolution and sampling. The components are:

- C1 : the 2.7 µm peak due to the (M)-OH stretching ;
- C2 : a small peak at 2.65 µm due to adsorbed water ;
- C3 : a 3 µm band associated with adsorbed water ;
- C4 : a band at 3.4 µm due to CH-stretching of organics.

The results for the He^+ implanted pellet for illumination angle $i = 0°$ are shown in Figure 6. We decided to show only the results from the He^+-implanted pellet, since we already saw that the Ar^+ case show little to no spectral changes upon ion bombardment. As a reminder, we are focusing on the changes in position of the hydration feature since the primary focus of this study is to determine possible compositional biases in the interpretation of the hydration feature's position. This value is representative of the type of hydrated silicate, while other parameters - such as band-depth of FWHD - instruct us about ion-implantation effects, such as amorphization.

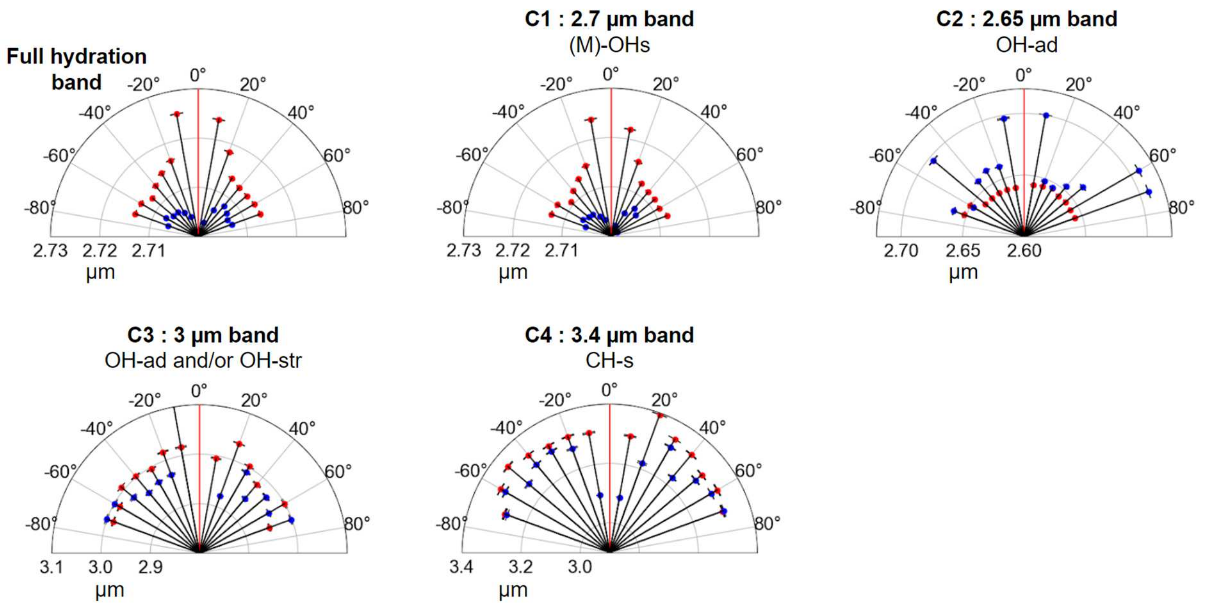

Figure 6. EMG fitting results on the He^+ implanted pellet in red and for the native pellet in blue, for the illumination angle $i = 0°$: evolution of the position of the hydration band and of the four components found by the model. C1= (M)-OH ; C2 = adsorbed-water (OH-as) ; C3 = adsorbed- and structural-water (OH-ad and OH-str) ; C4 = organics (CH-stretching) .

We observe that each component is somehow impacted by the irradiation and shows different bidirectional behaviors with respect to the non-bombarded sample. However, the changes in the position of the hydration band as a whole are dominated by the shift in position the $2.7\ \mu m$ peak, as this component represents the major contribution to this spectral feature. The position of each component shown here are not computed with the barycenter method described in section 3.2, but are instead a result of the EMG modeling. Note that, since our measurements were performed under air, the components related to the adsorbed water molecules detected at longer wavelengths are not relevant for the remote sensing implication of this work.

3.3 SEM imaging results

To further investigate the difference among the He^+ and Ar^+ implantation effects, we analyzed the state of the pellet's surface after bombardment with Scanning Electron Microscope (SEM) imaging. The acquired images are presented in Figure 7.

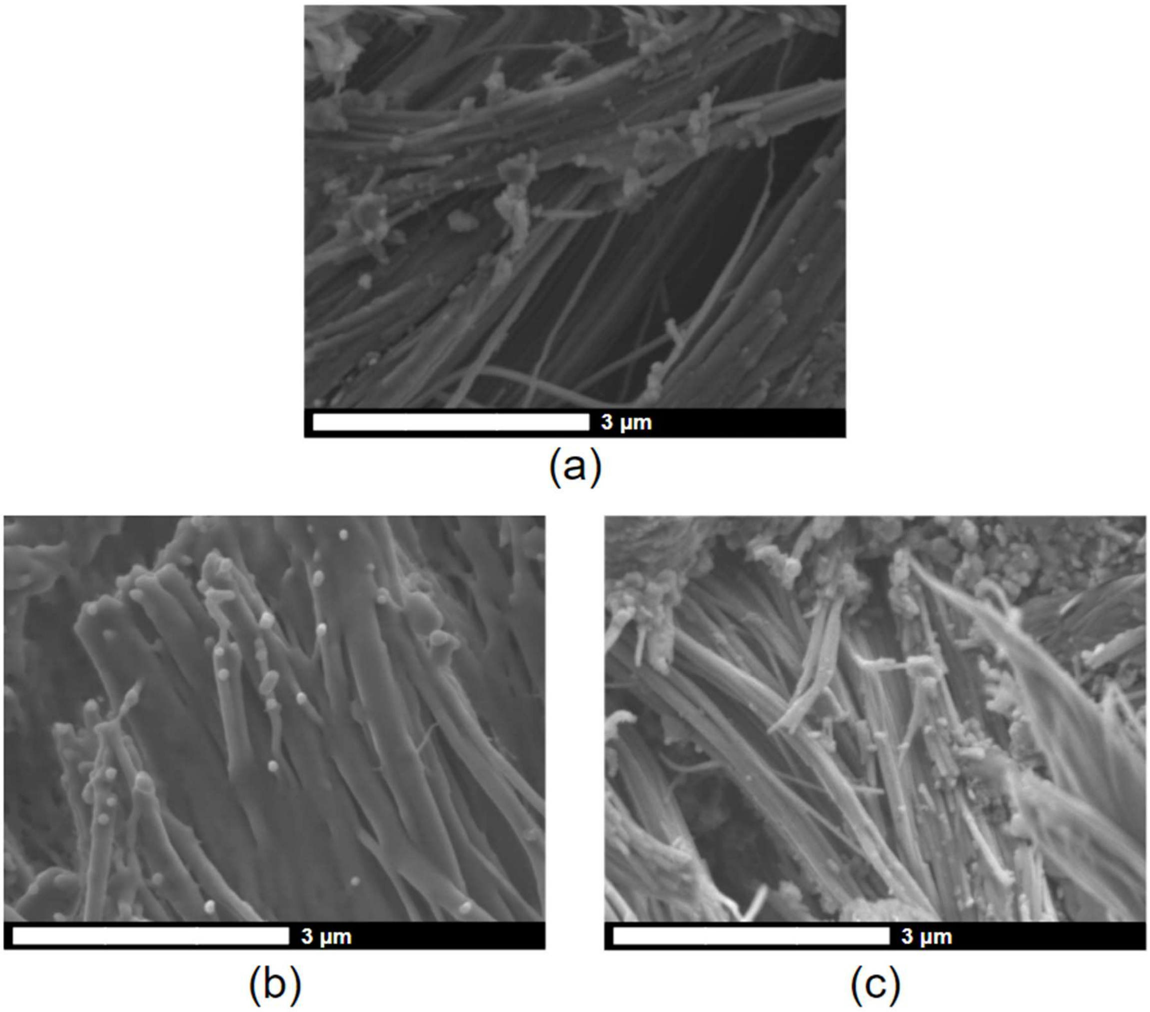

Figure 7. Scanning Electron Microscopy (SEM) images of the centers from the native Serpentine Rawhide pellet

(a), the Ar^+ bombarded pellet (b) and the He^+ bombarded one (c).
Images are acquired at 3kV with × *20 000* magnification.

No notable difference can be seen between the He^+ bombarded surface and the unirradiated one. However, there is a significant difference between these two and the Ar^+ bombarded surface. It appears that, even though the spectroscopic effects of the Ar^+ are difficult to detect, the heavy ion bombardment significantly alters the surface morphology, acting as a smoothing process, contrary to our He^+ bombarded pellet, which retains its grainy and frothy texture. The Ar^+ dulls and sometimes removes grainy morphological features that characterize the two other pellets. The removed features appear to be smaller than *10 nm* in size. The smoothing resulting from the Ar^+ bombardment has significantly altered the morphology of the pellet's surface, somewhat reducing the granularity of it.

4. DISCUSSION

Measurements on the He^+ bombarded pellet showed a clear shift in the position of the $2.7\,\mu m$ feature with respect to the non-implanted pellets as well as some slight broadening (see Figure B.2), consistent with ion-bombardment induced disordering, can also be seen. The spectral shift is due to chemical and physical changes induced by the ion implantation in the first hundreds of nanometers from the surface. The implantation depth in our samples was estimated by the SRIM software (Ziegler, Ziegler, and Biersack 2010) to be 0.310 ± 0.090 µm for He^+. However, we have seen that the amplitude of this spectral shift depends on the optical configuration of each measurement. Such diversity means that different effects are competing at the same time at different geometries. The scattering processes in a multi-layer compact structure are inherently complex. Two possible contributions and/or competing effects are volume (multiple) scattering and surface (specular) scattering.

Photons undergoing multiple scattering events in the volume of our sample are more sensible to the deeper layers of our sample. As the illumination angle increases, these photons will likely probe less deep. However, since the sample is observed at wavelengths of 2-3 µm, photons do not resolve layering at the scale of the implanted layer (approximately 0.3 µm as said above), thus mixing up both implanted and non-implanted material. The second contribution is related to specular scattering, which is sensitive to the optical properties of the utmost top layers of our samples. In specular reflection, the probing depth length would still mix ion-implanted and non-implanted matter, but we can qualitatively expect here to have a more prominent contribution from the ion-implanted one, compared to volume scattering. Hence, the specular component carries more information about the very top layer . This explains why specular geometrie in our dataset seem to better relay the effects of the ion-implantation, via the larger measured band-shift. The larger shift measured for $i = 0°$ at near-specular configuration compared to the other near-specular configurations could be explained taking in account the contribution of backscattered photons, which are also particularly sensitive to the surface layers of our samples.

All the patterns seen in our data may result from the combination of volume scattering, specular scattering and possibly backscattering. Overall, the observations suggest that measurements at high illumination angles of ion-implanted surfaces in near-specular configuration will be inherently slightly blue-shifted with respect to measurements done with a smaller illumination angle.

As we compare the effects of He^+ and Ar^+ implantation, we see that for the latter the effects on the hydration feature's position are barely detectable, independently from the optical configuration. The relative thickness of the layers altered by the two ions is noticeably distinct, as there is an order of magnitude difference between the penetration depth of He^+ and Ar^+ in serpentine (from SRIM code simulation : ~ 0.310 μm for He^+ and ~ 0.040 μm for Ar^+). Stopping-power profiles for these two ions, shown in (Brunetto et al. 2014), highlight the different energy-loss behavior, which explain the difference in the penetration depth of our ions. The SEM images in Figure 7 also highlight that the effects of Ar^+ are more prominent on the pellet's surface. A smaller penetration depth means that there's less implanted/modified matter to probe. The photon's optical path is dominated by native matter, the thickness of the Ar^+-implanted layer is much smaller than the wavelength of the probing photon, hence the difficulty in seeing the spectral effects of implanted matter. The altered layer is poorly relevant even at specular geometry. The light loss of surface granularity, due to Ar^+ sputtering, doesn't seem to play a particular role here.

Our study highlights that there is an optimal way to remotely detect ion implantation effects on Solar System surfaces: the spectral effects on hydrated surfaces can be better observed near specular configuration with near-nadir illumination angle. Incidence angles between 20 and 40° can also suffice, in case near-specular configuration is not achievable. These results can be put in the context of the Near-IR spectroscopic surveys carried out on the primitive hydrated bodies Ryugu and Bennu. In terms of remote sensing observation, the configuration that would maximize the spectral effects of space weathering on a primitive hydrated body would correspond to a measurement performed in nadir configuration (the detector onboard the orbiting craft is observing perpendicularly to the surface of the studied body) with a small phase angle φ associated with the measurement. However, it is relevant to point out that for this to work, the asteroidal surface to be analyzed would need to be particularly flat, which is not necessarily the case. For real case objects, surfaces are randomly distributed in orientation within the orbiter's observation footprint and in many cases are covered by regolith, which means that the specular components can be weaker and more dispersed than for our flat pellets: its contribution would be less easy to quantify. This sentence however has to be nuanced, since recent sample return missions, both Hayabusa missions and OSIRIS-REx, have shown that the idea of regolith covering the entirety of the surface of small airless bodies is a notion that needs to be revisited. Light regolith may escape the gravitational pull of small bodies, or flow and accumulate in certain regions. This means that, in the light of our study, for some geographical region, the specular component (which would always be present) would possibly be significant enough to carry sensible information for surface composition studies. Moreover, the spectral shift would probably be also more easily detected in spectroscopic surveys with a tighter field of view, dedicated to some particularly regular feature of interest. This would be the case for example for measurements conducted on fresh impact craters, boulders or fragments of boulders (which could be fractured due to temperature variations, hence exposing flat surfaces) or for rover/lander based measurements, where the chances of having the detector pixel filled with a smooth-enough surface would be larger. For now, these effects may be still hidden in the already acquired datasets, since the current trend consist of comparing different facets of a boulder at the same geometry of observation (see the study of the Otohime Saxon on Ryugu by Tatsumi et al. (2021)), instead of focusing on one facet at different geometries.

In the case of Ryugu and Bennu, their spectroscopic surveys were performed at varying geometric configurations on various regions. In Bennu's case, Deshapriya et al. (2021) show that crater regions on Bennu display a slightly blue-shifted hydration feature with respect to the average position of 2.74 μm (± 0.01) (Hamilton et al. 2019). This effect may point to the presence of less-weathered regions on the surface of Bennu, but in the light of this study, it would prove relevant to put in perspective these results with information regarding the measurament's geometry used for crater survey. Furthermore, this also means that the average position of the hydration feature on Bennu, 2.74 μm (± 0.01) (Hamilton et al. 2019), may be slightly blue-shifted due to the contribution of these blue-shifted regions. Taking into account this blue-shift in the OVIRS band centre would bring its attribution closer to the CI-CM group 2 type spectra described by (Takir et al. 2013), further supporting the CM2.1-2.2 petrologic-type attribution done by Hamilton et al.

In the case of Ryugu, the hydration feature has been extensively studied around the artificial SCI crater (Eri Tatsumi et al. 2019; Arakawa et al. 2020). Near-nadir configuration with phase angle $\varphi = 31.1°$ to $35.7°$ was kept during the various descent operations made to image the crater (Kitazato et al. 2021). Since phase angle was kept almost constant, the data acquired during the spectroscopic surveys of the SCI crater is, according to our findings, inherently less biased and easier to interpret, meaning that the slight peak variations of the hydration feature when comparing old and excavated terrains were indeed caused by chemical alterations at the surface, due to space weathering and/or thermal effects.

CONCLUSION

In order to better understand how the geometry of observation can affect remote sensing observations of space weathered primitive bodies, we measured the REFF function of He^{+} and Ar^{+} bombarded serpentine pellets, at varying illumination angles. We found that in the case of the He^{+} bombarded, the position of the $2.7\,\mu m$ hydration band, due to the stretching of hydroxyl groups connected to a metallic cation ((M)-OHs), shifts towards longer wavelengths as we approach specular configuration. This is due to chemical and physical changes induced by ion implantation effects in the first hundreds of nanometers, such as preferential amorphization of Mg-rich phyllosilicates or preferential sputtering of Mg (Hapke, Cassidy, and Wells 1975). The larger band-shift is measured at specular configuration, suggesting that the spectral signature of the implanted layer is carried by specular reflection. The diversity in the observed amplitude of the shift means that the main driver of this effect is the amount of specular reflection in the collected signal. Additional scattering effects will concur to the final result, but their contribution is more difficult to assess. Using a spectral deconvolution based on EMG profiles, we showed that the irradiation affects the various components of the hydration band independently. One can suggest that the variation of the band observed on the REFF measurements before and after irradiation are due to the alterations of the components themselves. Since the $2.7\,\mu m$ hydration band's position is characteristic of the composition of hydrated silicates, it is relevant to highlight its dependency with the angle of measurement, in order to avoid possible detection and interpretation biases.

A future work, currently in preparation, will focus on delving deeper in our sample, in order to study the chemical and physical changes induced by ion bombardment, using Transmission Electron Microscopy (TEM) imaging and Energy Dispersive Spectroscopy (TEM-EDS) to investigate the structural and chemical changes of the ion implanted samples.

ACKNOWLEDGMENTS

We thank O. Mivumbi, D. Ledu, C.O. Bacri, and P. Benoit-Lamaitrie for help and technical support with SIDONIE and INGMAR. INGMAR is a joint IAS-CSNSM (Orsay, France) facility funded by the P2IO LabEx (ANR-10-LABX-0038) in the framework Investissements d'Avenir (ANR-11-IDEX-0003-01). We would also like to thank A. Fadel for help and technical support with the SEM acquisitions. Finally, we thank both reviewers from the journal for their precious comments and questions. This work has been funded by the ANR project CLASSY (Grant ANR-17-CE31-0004-02) of the French Agence Nationale de la Recherche and by the Centre National d'Etudes Spatiales (CNES-France). The instrument SHADOWS was funded by the OSUG@2020 Labex (Grant ANR10 LABX56), by 'Europlanet 2020 RI', within the European Union's Horizon2020 research and innovation program (Grant N°654208) and by the Centre National d'Etudes Spatiales (CNES). HL thanks I-SITE ULNE and the MEL for funding. The electron microscopy works at the University of Lille were performed with the support of the Chevreul Institute, the European FEDER and Région Hauts-de-France.

APPENDIX A : SPECTRAL PARAMETERS

The spectral sampling for the acquired spectra was adjusted to be denser around the 2.7 µm band and looser where there were no bands of interest, to achieve a good compromise between quality of the measurement and time of acquisition. The spectral resolution was also adjusted with the same intent. In figure A1, both these spectral parameters and their variations along the spectra are shown.

(a)

Range [nm]	***Step [nm]***
400 → 1400	50
1400 → 1420	10
1450 → 2600	50
2600 → 2680	10
2680 → 2750	5
2750 → 2800	10
2800 → 2900	20
2900 → 3200	50
3200 → 4000	100

(b)

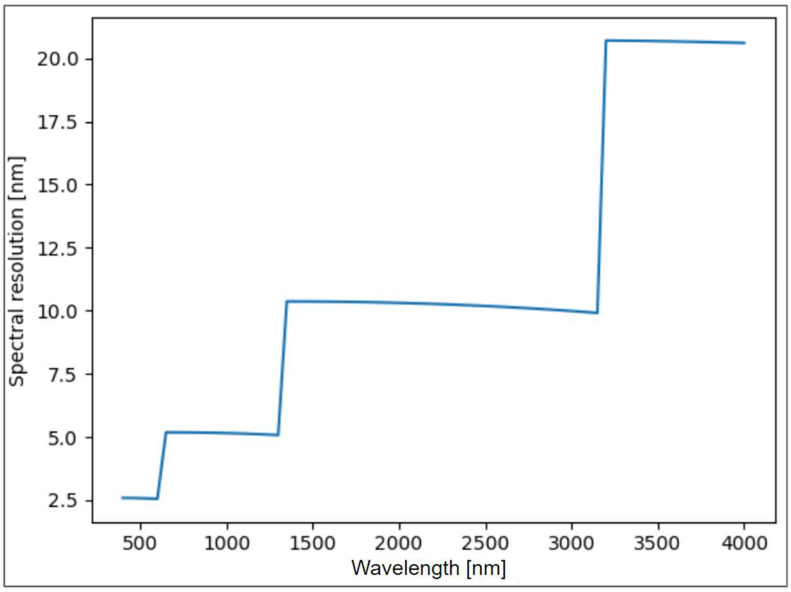

Figure A1. (a) Evolution of the spectral step and (b) Evolution of the spectral resolution

APPENDIX B : COMPLETE REFF DATASET

In Figure B1, the complete spectra of the entire REFF dataset for this experiment are shown. For high illumination angles i, when approaching specular configuration, spectral effects due to the domination of the specular components (explained under Figure 1) result in the alteration of the continuum shape, the reduction of weak features and the accentuation of the 1.4 and the 2.7 μm bands.

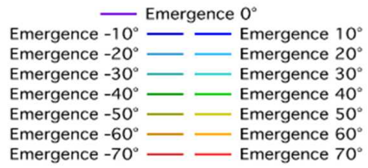

(a) Spectra from the **non-implanted pellet** at different observation geometries

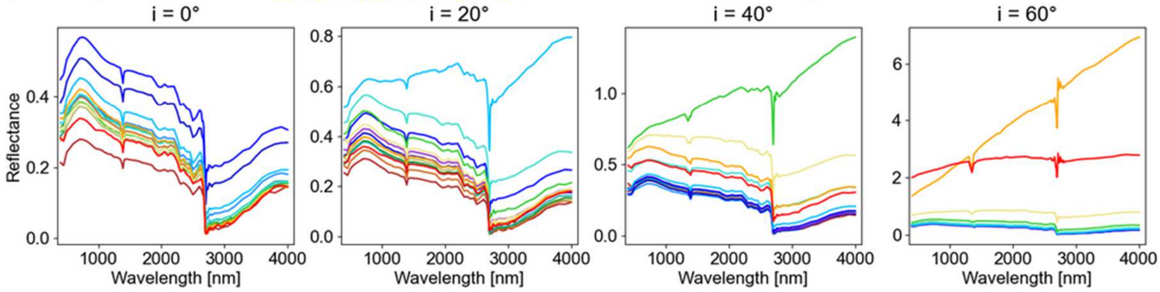

(b) Spectra from the **Ar+ implanted pellet** at different observation geometries

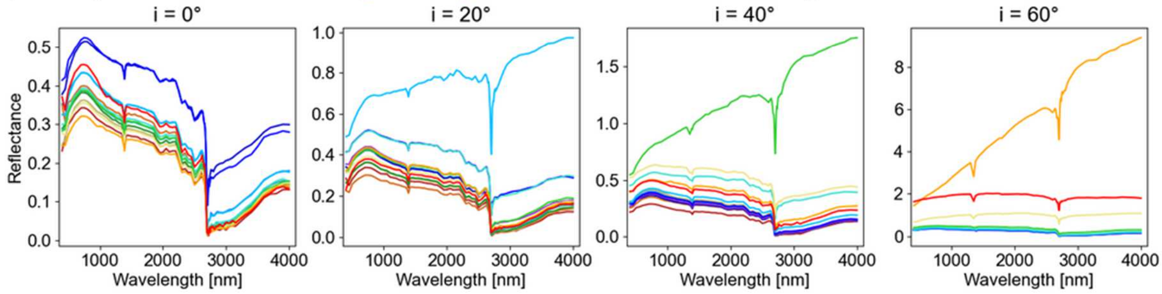

(c) Spectra from the **He+ implanted pellet** at different observation geometries

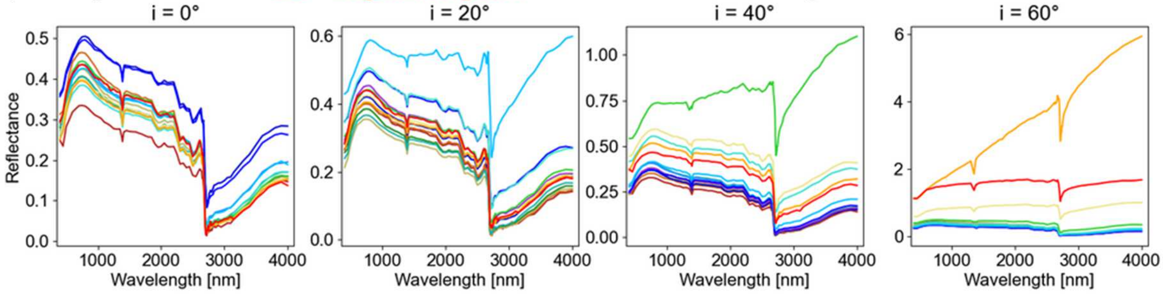

Figure B1. Complete REFF dataset

In Figure B2, the spectra centered on the hydration feature, after continuum removal, are shown. We can see that the band tends to shrink as we approach specular configuration. We are also able to appreciate the change in band-shape and observe the feature broadening upon ion-implantation, being much wider for the He^+ bombarded sample.

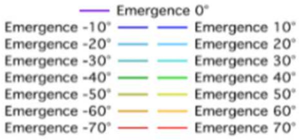

(a) Spectra from the **non-bombarded pellet** at different observation geometries

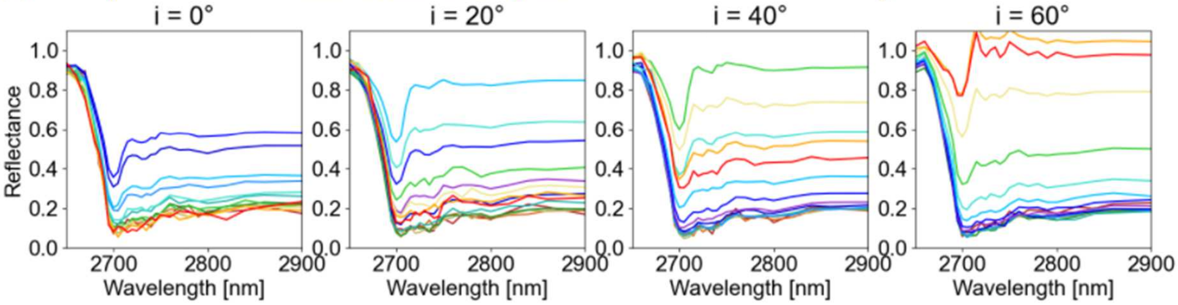

(b) Spectra from the **Ar+ implanted pellet** at different observation geometries

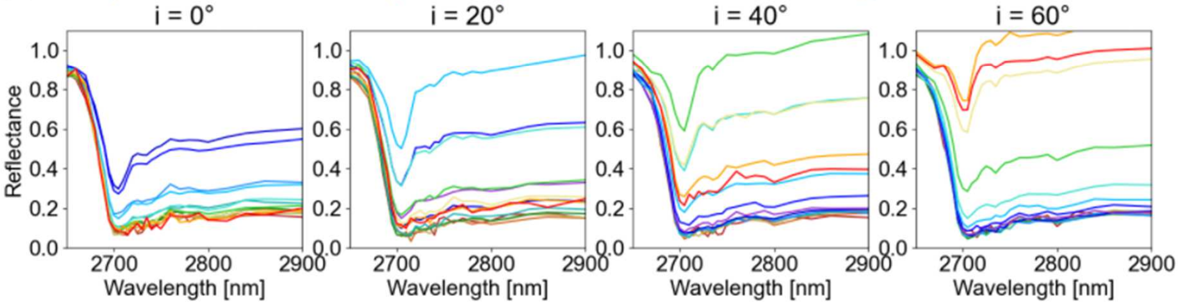

(c) Spectra from the **He+ implanted pellet** at different observation geometries

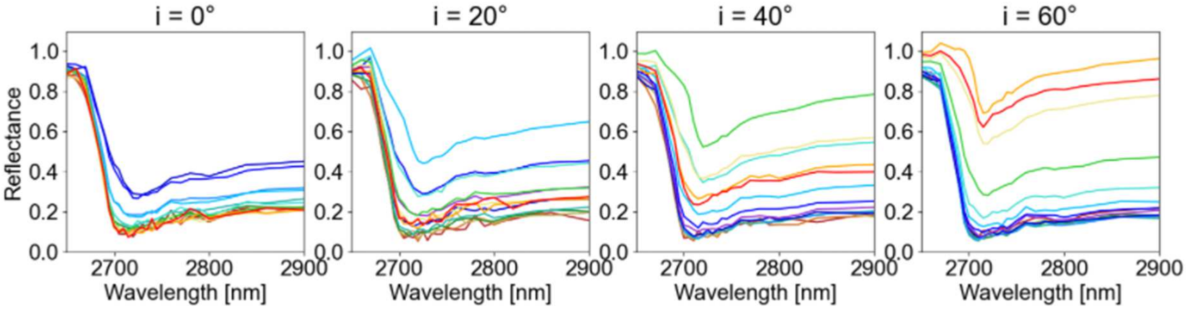

Figure B2. REFF dataset (complete dataset but restricted to 2.65-2.9 µm, after continuum removal)

APPENDIX C : EXPONENTIALLY MODIFIED GAUSSIAN (EMG) MODELING: COMPLETE BAND PARAMETERS TABLE

Table C1 presents the band parameters of the complete band and components derived from Figure 5. The position of the band is considered as the wavelength at which the reflectance is at its minimum value inside the band. The band depth is calculated as 1 – $R_{Band}/R_{Continuum}$, at the wavelength corresponding to the center of the band, and considering a linear continuum between the two inflection points of the band, R_{Band} being the measured reflectance at the position of minimum and $R_{Continuum}$ the reflectance of a linear continuum at the same wavelength. The errors are calculated following the procedure described in Potin et al. (2020a), considering 0.001 error bars and 500 simulated spectra. The errors are calculated, as described in Potin et al. (2020), based on the bootstrap statistical method. In this case, the fits are reproduced 500 times on the original data where a random fluctuation of 0.001 has been added. This method resulted in a large number of spectral parameters for each component, whose distribution is centered on the most probable value, considered here as the modeled band parameter, and with a FWHM corresponding to the error.

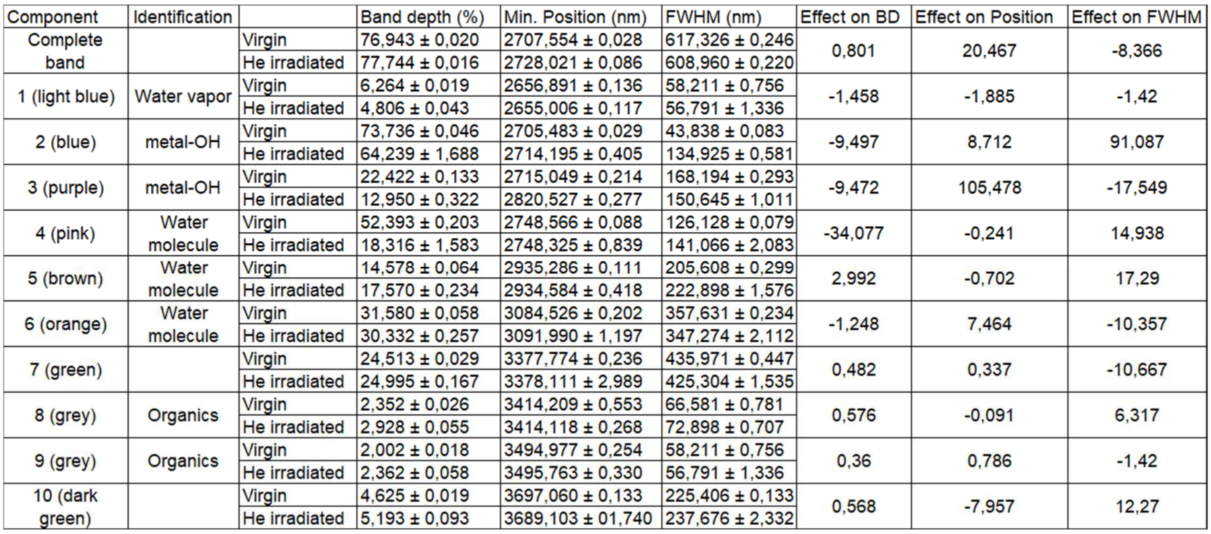

Component	Identification		Band depth (%)	Min. Position (nm)	FWHM (nm)	Effect on BD	Effect on Position	Effect on FWHM
Complete band		Virgin	76,943 ± 0,020	2707,554 ± 0,028	617,326 ± 0,246	0,801	20,467	-8,366
		He irradiated	77,744 ± 0,016	2728,021 ± 0,086	608,960 ± 0,220			
1 (light blue)	Water vapor	Virgin	6,264 ± 0,019	2656,891 ± 0,136	58,211 ± 0,756	-1,458	-1,885	-1,42
		He irradiated	4,806 ± 0,043	2655,006 ± 0,117	56,791 ± 1,336			
2 (blue)	metal-OH	Virgin	73,736 ± 0,046	2705,483 ± 0,029	43,838 ± 0,083	-9,497	8,712	91,087
		He irradiated	64,239 ± 1,688	2714,195 ± 0,405	134,925 ± 0,581			
3 (purple)	metal-OH	Virgin	22,422 ± 0,133	2715,049 ± 0,214	168,194 ± 0,293	-9,472	105,478	-17,549
		He irradiated	12,950 ± 0,322	2820,527 ± 0,277	150,645 ± 1,011			
4 (pink)	Water molecule	Virgin	52,393 ± 0,203	2748,566 ± 0,088	126,128 ± 0,079	-34,077	-0,241	14,938
		He irradiated	18,316 ± 1,583	2748,325 ± 0,839	141,066 ± 2,083			
5 (brown)	Water molecule	Virgin	14,578 ± 0,064	2935,286 ± 0,111	205,608 ± 0,299	2,992	-0,702	17,29
		He irradiated	17,570 ± 0,234	2934,584 ± 0,418	222,898 ± 1,576			
6 (orange)	Water molecule	Virgin	31,580 ± 0,058	3084,526 ± 0,202	357,631 ± 0,234	-1,248	7,464	-10,357
		He irradiated	30,332 ± 0,257	3091,990 ± 1,197	347,274 ± 2,112			
7 (green)		Virgin	24,513 ± 0,029	3377,774 ± 0,236	435,971 ± 0,447	0,482	0,337	-10,667
		He irradiated	24,995 ± 0,167	3378,111 ± 2,989	425,304 ± 1,535			
8 (grey)	Organics	Virgin	2,352 ± 0,026	3414,209 ± 0,553	66,581 ± 0,781	0,576	-0,091	6,317
		He irradiated	2,928 ± 0,055	3414,118 ± 0,268	72,898 ± 0,707			
9 (grey)	Organics	Virgin	2,002 ± 0,018	3494,977 ± 0,254	58,211 ± 0,756	0,36	0,786	-1,42
		He irradiated	2,362 ± 0,058	3495,763 ± 0,330	56,791 ± 1,336			
10 (dark green)		Virgin	4,625 ± 0,019	3697,060 ± 0,133	225,406 ± 0,133	0,568	-7,957	12,27
		He irradiated	5,193 ± 0,093	3689,103 ± 01,740	237,676 ± 2,332			

Table C1. Band parameters of the complete 3 µm band and components derived from the modelization shown on Figure 5. The colors to represent the components are similar to those in Figure 5.

REFERENCES

Amma, Shin-Ichi, Jiawei Luo, Carlo G. Pantano, and Seong H. Kim. 2015. "Specular Reflectance (SR) and Attenuated Total Reflectance (ATR) Infrared (IR) Spectroscopy of Transparent Flat Glass Surfaces: A Case Study for Soda Lime Float Glass." *Journal of*

Non-Crystalline Solids 428 (November): 189–96.

Arakawa, M., T. Saiki, K. Wada, K. Ogawa, T. Kadono, K. Shirai, H. Sawada, et al. 2020. “An Artificial Impact on the Asteroid (162173) Ryugu Formed a Crater in the Gravity-Dominated Regime.” *Science* 368 (6486): 67–71.

Brunetto, R., C. Lantz, Z. Dionnet, F. Borondics, A. Aléon-Toppani, D. Baklouti, M. A. Barucci, et al. 2018. “Hyperspectral FTIR Imaging of Irradiated Carbonaceous Meteorites.” *Planetary and Space Science* 158 (September): 38–45.

Brunetto, R., C. Lantz, D. Ledu, D. Baklouti, M. A. Barucci, P. Beck, L. Delauche, et al. 2014. “Ion Irradiation of Allende Meteorite Probed by Visible, IR, and Raman Spectroscopies.” *Icarus* 237 (July): 278–92.

Brunetto, R., C. Lantz, T. Nakamura, D. Baklouti, T. Le Pivert-Jolivet, S. Kobayashi, and F. Borondics. 2020. “Characterizing Irradiated Surfaces Using IR Spectroscopy.” *Icarus* 345 (July): 113722.

Brunetto, R., M. J. Loeffler, D. Nesvorný, S. Sasaki, and G. Strazzulla. 2015. “Asteroid Surface Alteration by Space Weathering Processes.” *Asteroids IV*. https://doi.org/10.2458/azu_uapress_9780816532131-ch031.

Christensen, P. R., V. E. Hamilton, G. L. Mehall, D. Pelham, W. O’Donnell, S. Anwar, H. Bowles, et al. 2018. “The OSIRIS-REx Thermal Emission Spectrometer (OTES) Instrument.” *Space Science Reviews* 214 (5): 87.

Clark, B. E., P. Lucey, P. Helfenstein, J. F. Bell Iii, C. Peterson, J. Veverka, T. Mcconnochie, et al. 2001. “Space Weathering on Eros: Constraints from Albedo and Spectral Measurements of Psyche Crater.” *Meteoritics & Planetary Science* 36 (12): 1617–37.

Clark, Beth Ellen, Bruce Hapke, Carlé Pieters, and Daniel Britt. 2002. “Asteroid Space Weathering and Regolith Evolution.” *Asteroids III* 585: 90086–90082.

Clark, Roger N., Trude V. V. King, Matthew Klejwa, Gregg A. Swayze, and Norma Vergo. 1990. “High Spectral Resolution Reflectance Spectroscopy of Minerals.” *Journal of Geophysical Research* 95 (B8): 12653.

De Sanctis, M. C., E. Ammannito, A. Raponi, S. Marchi, T. B. McCord, H. Y. McSween, F. Capaccioni, et al. 2015. “Ammoniated Phyllosilicates with a Likely Outer Solar System Origin on (1) Ceres.” *Nature* 528 (7581): 241–44.

Deshapriya, J. D. P., M. A. Barucci, E. B. Bierhaus, S. Fornasier, P. H. Hasselmann, F. Merlin, B. E. Clark, et al. 2021. “Spectral Analysis of Craters on (101955) Bennu.” *Icarus* 357 (March): 114252.

Grushka, E. 1972. “Characterization of Exponentially Modified Gaussian Peaks in Chromatography.” *Analytical Chemistry* 44 (11): 1733–38.

Hamilton, V. E., A. A. Simon, P. R. Christensen, D. C. Reuter, B. E. Clark, M. A. Barucci, N. E. Bowles, et al. 2019. “Evidence for Widespread Hydrated Minerals on Asteroid (101955) Bennu.” *Nature Astronomy* 3 (4): 332–40.

Hapke, B., W. Cassidy, and E. Wells. 1975. “Effects of Vapor-Phase Deposition Processes on the Optical, Chemical, and Magnetic Properties OE the Lunar Regolith.” *The Moon*. https://link.springer.com/article/10.1007/BF00567525.

Ishiguro, Masateru, Takahiro Hiroi, David J. Tholen, Sho Sasaki, Yuji Ueda, Tokuhiro Nimura, Masanao Abe, et al. 2007. “Global Mapping of the Degree of Space Weathering on Asteroid 25143 Itokawa by Hayabusa/AMICA Observations.” *Meteoritics & Planetary Science* 42 (10): 1791–1800.

Iwata, Takahiro, Kohei Kitazato, Masanao Abe, Makiko Ohtake, Takehiko Arai, Tomoko Arai, Naru Hirata, et al. 2017. “NIRS3: The Near Infrared Spectrometer on Hayabusa2.” *Space Science Reviews* 208 (1): 317–37.

Jones, Thomas D., Larry A. Lebofsky, John S. Lewis, and Mark S. Marley. 1990. “The Composition and Origin of the C, P, and D Asteroids: Water as a Tracer of Thermal

Evolution in the Outer Belt." *Icarus* 88 (1): 172–92.

King, A. J., P. F. Schofield, K. T. Howard, and S. S. Russell. 2015. "Modal Mineralogy of CI and CI-like Chondrites by X-Ray Diffraction." *Geochimica et Cosmochimica Acta* 165 (September): 148–60.

Kitazato, K., R. E. Milliken, T. Iwata, M. Abe, M. Ohtake, S. Matsuura, T. Arai, et al. 2019. "The Surface Composition of Asteroid 162173 Ryugu from Hayabusa2 near-Infrared Spectroscopy." *Science* 364 (6437): 272–75.

Kitazato, K., R. E. Milliken, T. Iwata, M. Abe, M. Ohtake, S. Matsuura, Y. Takagi, et al. 2021. "Thermally Altered Subsurface Material of Asteroid (162173) Ryugu." *Nature Astronomy*, January. https://doi.org/10.1038/s41550-020-01271-2.

Lantz, C., R. Brunetto, M. A. Barucci, E. Dartois, J. Duprat, C. Engrand, M. Godard, D. Ledu, and E. Quirico. 2015. "Ion Irradiation of the Murchison Meteorite: Visible to Mid-Infrared Spectroscopic Results." *Astronomy & Astrophysics*. https://doi.org/10.1051/0004-6361/201425398.

Lantz, C., R. Brunetto, M. A. Barucci, S. Fornasier, D. Baklouti, J. Bourçois, and M. Godard. 2017. "Ion Irradiation of Carbonaceous Chondrites: A New View of Space Weathering on Primitive Asteroids." *Icarus* 285 (March): 43–57.

Lauretta, D. S., S. S. Balram-Knutson, E. Beshore, W. V. Boynton, C. Drouet d'Aubigny, D. N. DellaGiustina, H. L. Enos, et al. 2017. "OSIRIS-REx: Sample Return from Asteroid (101955) Bennu." *Space Science Reviews* 212 (1): 925–84.

Madejová, J., W. P. Gates, and S. Petit. 2017. "IR Spectra of Clay Minerals." *Developments in Clay Science*. https://doi.org/10.1016/b978-0-08-100355-8.00005-9.

Milliken, Ralph E., John F. Mustard, François Poulet, Denis Jouglet, Jean-Pierre Bibring, Brigitte Gondet, and Yves Langevin. 2007. "Hydration State of the Martian Surface as Seen by Mars Express OMEGA: 2. H2O Content of the Surface." *Journal of Geophysical Research* 112 (E8). https://doi.org/10.1029/2006je002853.

Mooney, T., and R. F. Knacke. 1985. "Optical Constants of Chlorite and Serpentine between 2.5 and 50 µm." *Icarus* 64 (3): 493–502.

Müller, Christian Menno, Bobby Pejcic, Lionel Esteban, Claudio Delle Piane, Mark Raven, and Boris Mizaikoff. 2014. "Infrared Attenuated Total Reflectance Spectroscopy: An Innovative Strategy for Analyzing Mineral Components in Energy Relevant Systems." *Scientific Reports* 4 (October): 6764.

Ockman, Nathan. 1958. "The Infra-Red and Raman Spectra of Ice." *Advances in Physics* 7 (26): 199–220.

Potin, Sandra, Olivier Brissaud, Pierre Beck, Bernard Schmitt, Yves Magnard, Jean-Jacques Correia, Patrick Rabou, and Laurent Jocou. 2018. "SHADOWS: A Spectro-Gonio Radiometer for Bidirectional Reflectance Studies of Dark Meteorites and Terrestrial Analogs: Design, Calibrations, and Performances on Challenging Surfaces." *Applied Optics* 57 (28): 8279–96.

Potin, S., P. Beck, B. Schmitt, and F. Moynier. 2019. "Some Things Special about NEAs: Geometric and Environmental Effects on the Optical Signatures of Hydration." *Icarus* 333 (November): 415–28.

Potin, S., S. Manigand, P. Beck, C. Wolters, and B. Schmitt. 2020. "A Model of the 3-µm Hydration Band with Exponentially Modified Gaussian (EMG) Profiles: Application to Hydrated Chondrites and Asteroids." *Icarus* 343 (June): 113686.

Rivkin, A. S., E. S. Howell, F. Vilas, and L. A. Lebofsky. 2002. "Hydrated Minerals on Asteroids: The Astronomical Record." *Asteroids III* 1: 235–53.

Rubino, S., C. Lantz, D. Baklouti, and H. Leroux. 2020. "Space Weathering Affects the Remote Near-IR Identification of Phyllosilicates." *The Planetary Report*. https://iopscience.iop.org/article/10.3847/PSJ/abb94c/meta.

RYSKIN, and Y. I. 1974. “The Vibrations of Protons in minerals:Hydroxyl, Water and Ammonium.” *The Infrared Spectra of Minerals*, 137–82.

Takir, Driss, Joshua P. Emery, Harry Y. Mcsween, Charles A. Hibbitts, Roger N. Clark, Neil Pearson, and Alian Wang. 2013. “Nature and Degree of Aqueous Alteration in CM and CI Carbonaceous Chondrites.” *Meteoritics & Planetary Science*. https://doi.org/10.1111/maps.12171.

Tatsumi, Eri, Toru Kouyama, Hidehiko Suzuki, Manabu Yamada, Naoya Sakatani, Shingo Kameda, Yasuhiro Yokota, et al. 2019. “Updated Inflight Calibration of Hayabusa2’s Optical Navigation Camera (ONC) for Scientific Observations during the Cruise Phase.” *Icarus* 325 (June): 153–95.

Tatsumi, E., C. Sugimoto, L. Riu, S. Sugita, T. Nakamura, T. Hiroi, T. Morota, et al. 2021. “Collisional History of Ryugu’s Parent Body from Bright Surface Boulders.” *Nature Astronomy* 5 (1): 39–45.

Usui, Fumihiko, Sunao Hasegawa, Takafumi Ootsubo, and Takashi Onaka. 2018. “AKARI/IRC near-Infrared Asteroid Spectroscopic Survey: AcuA-Spec.” *Publications of the Astronomical Society of Japan* 71 (1). https://doi.org/10.1093/pasj/psy125.

Watanabe, Sei-Ichiro, Yuichi Tsuda, Makoto Yoshikawa, Satoshi Tanaka, Takanao Saiki, and Satoru Nakazawa. 2017. “Hayabusa2 Mission Overview.” *Space Science Reviews* 208 (1): 3–16.

Ziegler, James F., M. D. Ziegler, and J. P. Biersack. 2010. “SRIM – The Stopping and Range of Ions in Matter (2010).” *Nuclear Instruments and Methods in Physics Research Section B: Beam Interactions with Materials and Atoms*. https://doi.org/10.1016/j.nimb.2010.02.091.